

High Order Curvilinear Finite Elements for Elastic-Plastic Lagrangian Dynamics [☆]

Veselin A. Dobrev^a, Tzanio V. Kolev^a, Robert N. Rieben^b

^a*Center for Applied Scientific Computing, Lawrence Livermore National Laboratory*

^b*Weapons and Complex Integration, B-Division, Lawrence Livermore National Laboratory*

Abstract

This paper presents a high-order finite element method for calculating elastic-plastic flow on moving curvilinear meshes and is an extension of our general high-order curvilinear finite element approach for solving the Euler equations of gas dynamics in a Lagrangian frame [1, 2]. In order to handle transition to plastic flow, we formulate the stress-strain relation in rate (or incremental) form and augment our semi-discrete equations for Lagrangian hydrodynamics with an additional evolution equation for the deviatoric stress which is valid for arbitrary order spatial discretizations of the kinematic and thermodynamic variables. The semi-discrete equation for the deviatoric stress rate is developed for 2D planar, 2D axisymmetric and full 3D geometries. For each case, the strain rate is approximated via a collocation method at zone quadrature points while the deviatoric stress is approximated using an L_2 projection onto the thermodynamic basis. We apply high order, energy conserving, explicit time stepping methods to the semi-discrete equations to develop the fully discrete method. We conclude with numerical results from an extensive series of verification tests that demonstrate several practical advantages of using high-order finite elements for elastic-plastic flow.

Keywords: Elastic-plastic flow, Lagrangian hydrodynamics, High-order finite element methods

1. Introduction and Motivation

The physical evolution of high velocity elastic, plastic and fluid motion can be generally described by the Euler equations of compressible hydrodynamics. Typically, the Euler equations are used to model gas dynamics where the stresses are governed by a scalar pressure field defined by an equation of state (EOS). With an appropriate definition of the stress tensor and a material constitutive model, they can also be used to model complex shock wave interactions with elastic-plastic materials [3, 4]. Our research is concerned with the solution of these equations on general, unstructured 2D and 3D computational domains using high

[☆]This work performed under the auspices of the U.S. Department of Energy by Lawrence Livermore National Laboratory under Contract DE-AC52-07NA27344, LLNL-JRNL-567119

Email addresses: `dobrev1@llnl.gov` (Veselin A. Dobrev), `kolev1@llnl.gov` (Tzanio V. Kolev), `riebe1@llnl.gov` (Robert N. Rieben)

order finite element methods. We focus on Lagrangian numerical methods, where the equations are discretized and solved on a mesh that moves with the material velocity. As shown in [1, 2, 5], high order Lagrangian methods result in curvilinear meshes which accurately capture features of the material flow. Specifically, our goal is to solve the following system of conservation laws:

$$\text{Momentum Conservation: } \rho \frac{dv}{dt} = \nabla \cdot \sigma, \quad (1)$$

$$\text{Mass Conservation: } \frac{1}{\rho} \frac{d\rho}{dt} = -\nabla \cdot v, \quad (2)$$

$$\text{Energy Conservation: } \rho \frac{de}{dt} = \sigma : \nabla \vec{v}, \quad (3)$$

$$\text{Equation of Motion: } \frac{dx}{dt} = \vec{v}, \quad (4)$$

which involves the material derivative $\frac{d}{dt}$, the kinematic variables for the fluid velocity v and position x , and the thermodynamic variables for the density ρ , the (specific) internal energy e and the total stress tensor σ of the material [6, 7].

A constitutive (or material) model is required to define the total stress tensor σ to the state of the material, which includes the hydrodynamic variables ρ , e , v and x . In the simple case of ideal gas dynamics, the total stress is an isotropic tensor defined by a scalar pressure field $\sigma = -pI$ which is determined by the equation of state

$$p = EOS(\rho, e) = (\gamma - 1)\rho e, \quad (5)$$

where $\gamma > 1$ is the constant adiabatic index of the ideal gas. In general, the EOS of a material can be given in analytic form derived from theoretical and/or empirical considerations, or in the form of experimentally determined tabulated data.

For elastic materials, the total stress tensor σ is no longer isotropic, but it is still desirable to decompose the total stress into an isotropic component which is defined via the EOS and a *deviatoric* component, denoted by s , resulting in a so-called material “strength model”

$$\sigma = -pI + s. \quad (6)$$

The stress deviator tensor, s , is then treated as a new state variable whose evolution will be described by an appropriate constitutive relation. The tensor s is symmetric and has the following set of invariants:

$$J1 \equiv \text{Tr}(s) = 0, \quad (7)$$

$$J2 \equiv -\frac{1}{2} (\text{Tr}(s)^2 - \text{Tr}(s^2)) = \frac{1}{2} \text{Tr}(s^2), \quad (8)$$

$$J3 \equiv \det(s). \quad (9)$$

Because the stress deviator tensor is traceless via (7), it describes a state of *pure shear* [8].

There is a wide range of mathematical models aimed at describing the behavior of materials in the elastic and the transition to plastic regimes. These include the classical work of Wilkins [3], and more recent approaches described in [9] as well as the overview provided in the recent paper [10] where the authors also discuss some of the disadvantages of

the classical models. From a computational point of view, there is also a wide range of discretization methods based on different elastic-plastic models. Such approaches include Lagrangian staggered grid schemes [3, 11, 12], Eulerian methods [13, 14], free-Lagrange methods [15], Lagrangian finite element [16] and cell centered methods [17, 10].

In this work, we focus on the classical hypoelastic approach of [3] which is based on an incremental stress-strain relation in conjunction with the von Mises yield condition which is discretized using the method of radial return for projecting the deviatoric stresses back onto the yield surface. This results in an additional evolution equation for the stress deviator that needs to be solved in conjunction with the conservation laws of (1)–(4).

The novelty of our approach lies in the use of a high order, curvilinear finite element discretization of the stress deviator evolution equation and its coupling with the corresponding high order discretization of the conservation laws of (1)–(4). We achieve this by representing each component of the stress deviator, s , in the finite element space used for the discretization of the thermodynamic variables. Using this representation, we then derive a semi-discrete equation for the stress deviator evolution which we develop for 2D planar, 2D axisymmetric and full 3D geometries. To ensure high order accuracy in the time integration of the semi-discrete evolution equations, we apply high order, energy conserving, explicit time stepping methods to develop the fully discrete method. We also introduce a general approach for applying radial return to the stress deviator during each sub-stage of the high order time integration methods.

The remainder of the paper is organized as follows. In Section 2 we recall some basic facts about linear elastic and plastic material deformations. In Section 3 we describe the incremental stress-strain relation that we use and define the deviatoric stress evolution equation. In Section 4 we introduce finite element notation and develop a semi-discrete form of the deviatoric stress evolution equation in 2D planar, 2D axisymmetric and full 3D geometries. We also develop a general high order, explicit time discretization approach for integrating this equation, along with the other semi-discrete conservation laws, in time. In Section 5, we present an extensive set of numerical results that demonstrate the robustness of our algorithm with respect to symmetry and energy conservation on a range of elastic-plastic test problems. Finally, we summarize our experience and draw some conclusions in Section 6.

2. Linear Elastic and Plastic Deformation

Linear elastic materials resist change in shape, which is often referred to as a material’s “strength.” Consider a volume of material with initial spatial coordinates \tilde{x} and deformed coordinates x . Define the displacement vector field as

$$u \equiv x - \tilde{x}.$$

In the limit of small displacements, the strain tensor is given by

$$\epsilon \equiv \frac{1}{2}(\nabla u + u \nabla). \quad (10)$$

The *deviatoric* strain tensor is defined as

$$E = \epsilon - \frac{1}{3} \text{Tr}(\epsilon) I = \epsilon - \frac{1}{3} (\nabla \cdot u) I.$$

For linear elastic materials, the constitutive relationship between the deviatoric stress tensor and the deviatoric strain tensor is

$$s = 2\mu_s E, \quad (11)$$

where μ_s is the shear modulus (or modulus of rigidity) which can, in general, depend on other state variables such as density and internal energy [18].

Certain solids, like many metals in a wide range of conditions, often behave essentially as linear elastic materials unless the applied stress exceeds some critical value known as the “yield stress” which is denoted Y . Above this threshold, materials become both non-linear and non-elastic, leading to permanent deformation and sometimes material failure (such as fracture). The term elastic-plastic is used to describe the state beyond which further distortion results in plastic flow, in which no additional elastic energy is stored and only plastic work is done. When the material is loaded beyond this state, which is modeled with the yield stress, and subsequently unloaded, only the elastic distortion energy is recovered; the work done during the plastic phase (and accumulated in the plastic strain) is not recovered [19].

In order to determine if the applied stress is great enough to cause yielding, we use the von Mises yield condition, which is based on the $J2$ invariant from (8). Specifically, the condition is

$$J2 \leq \frac{1}{3}Y^2. \quad (12)$$

This inequality defines the “yield surface” of a material. In the discretization of the elastic-plastic equations this inequality can be enforced at a given time step using a process known as *radial return* [3, 20] which we describe later.

3. Deviatoric Stress Evolution Equation

Once a material has transitioned from linear elastic to non-linear plastic flow, we can no longer define a meaningful absolute strain relative to some initial configuration at time $t = 0$ via (10). Adopting a hypoelastic formulation, (11) can be modified to be in incremental form as the relation between a stress rate and a strain rate [4]. In the limit of small displacements, the strain *rate* tensor is given by

$$\dot{\epsilon} \equiv \frac{1}{2}(\nabla v + v\nabla), \quad (13)$$

and the deviatoric strain rate tensor is defined as

$$\dot{E} = \dot{\epsilon} - \frac{1}{3}(\nabla \cdot v)I.$$

It is essential for the rate dependent elastic-plastic constitutive equation to be frame invariant (or objective); however, frame invariance of the stress rate is not guaranteed even if the strain rate is frame invariant [21]. Consider a general rotation process applied to the stress deviator tensor

$$s' = RsR^T,$$

for some orthogonal matrix R such that $RR^T = I$. Applying the material derivative to s' to get a stress rate, we obtain

$$\frac{ds'}{dt} = \frac{dR}{dt}sR^T + R\frac{ds}{dt}R^T + Rs\frac{dR^T}{dt},$$

which means that

$$\frac{ds'}{dt} \neq R\frac{ds}{dt}R^T$$

and the stress rate is not frame invariant unless the rate of rotation is zero, i.e. R is constant.

There are numerous frame invariant (or objective) stress rate formulations in the literature on continuum mechanics. The simplest, and perhaps the most commonly used is the Jaumann rate, given by

$$\dot{s} \equiv \frac{ds}{dt} + (s\dot{\omega} - \dot{\omega}s), \quad (14)$$

where, in the limit of small rotations, the rotation rate (or spin) tensor is given by

$$\dot{\omega} \equiv \frac{1}{2}(\nabla v - v\nabla). \quad (15)$$

Using the Jaumann stress rate definition of (14), we can write the deviatoric constitutive relation of (11) in rate form as

$$\frac{ds}{dt} = 2\mu_s\dot{E} - (s\dot{\omega} - \dot{\omega}s). \quad (16)$$

In order to ensure that the deviatoric stress satisfies the plastic yield condition (12) we need to additionally modify the above equation by subtracting the plastic strain rate $\dot{\epsilon}^p$ from the deviatoric strain rate \dot{E} , see [10]

$$\frac{ds}{dt} = 2\mu_s(\dot{E} - \dot{\epsilon}^p) - (s\dot{\omega} - \dot{\omega}s). \quad (17)$$

The plastic strain rate $\dot{\epsilon}^p$ is defined as

$$\dot{\epsilon}^p = \begin{cases} (\dot{\epsilon} : s)/(s : s)s & \text{if } J2 = Y^2/3 \text{ and } \dot{\epsilon} : s > 0, \\ 0 & \text{otherwise.} \end{cases}$$

Equation (17) represents the evolution equation for the deviatoric stress which will need to be solved in conjunction with the conservation laws of (1)–(4). Alternatively, instead of discretizing (17) in time, one may discretize (16) while performing a radial return step after each time sub-step thus ensuring that the plastic yield condition (12) is always satisfied. In our discrete algorithm we utilize the latter approach.

Whenever plastic yielding in a material occurs ($\dot{\epsilon}^p > 0$), a permanent strain is accumulated in the material. This permanent deformation can be measured by the *equivalent plastic strain* (EPS) defined as

$$\bar{\epsilon}^p = \int_{t_0}^t \sqrt{\frac{2}{3}(\dot{\epsilon}^p : \dot{\epsilon}^p)} dt,$$

which can be used to define work-hardening models for the yield stress: $Y = Y(\bar{\epsilon}^p)$.

4. Finite Element Discretization

In this section we derive and discuss a finite element-based numerical approximation scheme for the Euler equations (1)–(4) in the case of general elastic-plastic materials. The presentation follows the general semi-discrete Lagrangian discretization method from [1] (and [2] for the axisymmetric case), to which we refer for additional details.

4.1. Semi-Discrete Formulation

We first discuss the spatial approximation of the continuum equations giving rise to our semi-discrete approximation method. The fully-discrete method, where we also discretize the equations in time, will be presented in the following section.

We start from a finite element mesh on our computational domain $\Omega(t)$ at initial time $t = t_0$ consisting of zones (or elements) $\{\Omega_z(t_0)\}$. To more accurately represent the naturally developing curvature in the flow, we use high-order curvilinear zones which are described through the locations of high-order particles (or control points) that are tracked by the semi-discrete algorithm. Specifically, the current position at time t of a particle at an initial position $\tilde{x} \in \tilde{\Omega} \equiv \Omega(t_0)$ is discretized using the expansion

$$x(\tilde{x}, t) \approx \sum_{i=1}^{N_v} \mathbf{x}_i(t) w_i(\tilde{x}) = \mathbf{x}(t)^T \mathbf{w}(\tilde{x}), \quad (18)$$

where $\mathbf{x}(t)$ is an unknown time-dependent vector of coefficients in the kinematic basis $\{w_i\}_{i=1}^{N_v}$, and \mathbf{w} is a column vector of all the basis functions $\{w_i\}$. The kinematic basis functions are continuous and are used to discretize both the position and the velocity fields. This way, the discrete velocity can be directly used to move the mesh and automatically satisfies the equation of motion:

$$v(\tilde{x}, t) \approx \sum_i \frac{d\mathbf{x}_i}{dt}(t) w_i(\tilde{x}) = \mathbf{v}(t)^T \mathbf{w}(\tilde{x}), \quad \text{i.e.} \quad \mathbf{v} = \frac{d\mathbf{x}}{dt}. \quad (19)$$

The curvilinear zones at time t are reconstructed as

$$\Omega_z(t) = \{x = \Phi_z(\hat{x}, t) : \hat{x} \in \hat{\Omega}_z\}, \quad (20)$$

where Φ_z is the parametric mapping from the reference element

$$\Phi_z(\hat{x}, t) = \sum_{i=1}^{N_v} x_{z,i}(t) \hat{\eta}_i(\hat{x}). \quad (21)$$

Here $\{\hat{\eta}_i\}_{i=1}^{N_v}$ are the nodal finite element basis functions which are used to define the basis function $\{w_i\}$ through Cartesian products on the standard reference zone $\hat{\Omega}_z$ (the unit square/cube in 2D/3D). The Jacobian of the parametric mapping is denoted by $\mathbf{J}_z = \nabla_{\hat{x}} \Phi_z$.

We eliminate the density field from our numerical algorithm through the concept of *strong mass conservation* (see [1]), which states that the total mass in any moving volume does not change in time. This can be reduced to the equation

$$\rho(t) |\mathbf{J}_z(t)| = \rho(t_0) |\mathbf{J}_z(t_0)|, \quad (22)$$

which we assume to hold on the reference element at any time t .

To discretize the internal energy e and the components of the stress deviator tensor s_{ij} , we introduce a thermodynamic finite element space with a basis $\{\phi_i\}_{j=1}^{N_\varepsilon}$. We then use the finite element expansions

$$e(\tilde{x}, t) \approx \sum_i \mathbf{e}_i(t) \phi_i(\tilde{x}), \quad (23)$$

$$s_{ij}(\tilde{x}, t) \approx \sum_k (\mathbf{s}_{ij})_k(t) \phi_k(\tilde{x}), \quad (24)$$

where $\mathbf{e}(t)$ and $\mathbf{s}_{ij}(t)$ are unknown time-dependent coefficient vectors. We choose a finite element representation for the stress deviator components (as opposed to direct point-wise evaluation), since the finite element functional representation fits more naturally in our framework. We furthermore use the same discretization space for all non-kinematic unknowns, since this leads to several practical advantages, including reduced memory requirements and the possibility to reuse finite element components computed in the internal energy update.

The functions ϕ_i are typically discontinuous and are of one order lower compared to the kinematic space on the reference element, i.e. a typical pair of kinematic and thermodynamic discretization spaces is Q_k - Q_{k-1} , $k \geq 1$, corresponding to continuous w_i with $\hat{\eta}_i \in Q_k$ and discontinuous ϕ_i with $\hat{\phi}_i \in Q_{k-1}$. Note also that we treat all of the unknown fields as *functions* varying within each zone: the position, velocity, internal energy and stress deviator components are expanded as finite element fields, while the density and the pressure are general (non-finite element) functions given by (22) and the EOS (5).

Our semi-discrete approximation of (1)–(4) is based on weak variational formulations using the above kinematic and thermodynamic finite element spaces. The derivation is similar to [1]: based on the kinematic and thermodynamic *mass matrices*

$$(\mathbf{M}_V)_{ij} = \int_{\Omega(t)} \rho w_i w_j \quad \text{and} \quad (\mathbf{M}_\varepsilon)_{ij} = \int_{\Omega(t)} \rho \phi_i \phi_j, \quad (25)$$

as well as the generalized *force matrix*

$$\mathbf{F}_{ij} = \int_{\Omega(t)} (\sigma : \nabla w_i) \phi_j, \quad (26)$$

we define the following semi-discrete approximation to the Euler equations:

$$\text{Semi-Discrete Momentum Conservation: } \mathbf{M}_V \frac{d\mathbf{v}}{dt} = -\mathbf{F} \cdot \mathbf{1}, \quad (27)$$

$$\text{Semi-Discrete Energy Conservation: } \mathbf{M}_\varepsilon \frac{d\mathbf{e}}{dt} = \mathbf{F}^T \cdot \mathbf{v}, \quad (28)$$

$$\text{Semi-Discrete Stress Rate: } \mathbf{M}_\varepsilon \frac{d\mathbf{s}_{ij}}{dt} = \mathbf{g}_{ij}, \quad (29)$$

$$\text{Semi-Discrete Equation of Motion: } \frac{d\mathbf{x}}{dt} = \mathbf{v}. \quad (30)$$

Compared to [1], we have an additional equation for the components of the deviatoric stress, which is based on a density-weighted projection of (16) onto the discontinuous thermodynamic space:

$$(\mathbf{g}_{ij})_k = \int_{\Omega(t)} (\rho g_{ij}) \phi_k, \quad (31)$$

where the stress deviator tensor *rate function* is defined using (16) as

$$g(s, v, \mu_s) \equiv \mu_s \left((\nabla v + v \nabla) - \frac{2}{3} (\nabla \cdot v) I \right) - \frac{1}{2} (s (\nabla v - v \nabla) - (\nabla v - v \nabla) s). \quad (32)$$

The density-weighted projection (28) of the above stress deviator rate function is the most natural way to define the stress rate in finite element terms. This particular choice has the practical advantage that it allows us to reuse the thermodynamic mass matrix \mathbf{M}_ε in the stress deviator update.

Since the stress deviator tensor is symmetric, we only need to compute 6 independent values in 3D $(s_{xx}, s_{yy}, s_{zz}, s_{xy}, s_{xz}, s_{yz})$ and 3 independent values in 2D (s_{xx}, s_{yy}, s_{xy}) . We emphasize that s , v , μ_s and the velocity gradient ∇v are treated as *functions* that vary inside of a zone and are evaluated at quadrature points in the integral definition of (31). The stress deviator, s , in (32) is computed using the finite element representation of (24) while the velocity gradient is computed by differentiating the expansion (19) with respect to the physical coordinate x .

In the case of elastic-plastic flow, the von Mises yield condition (12) is enforced using the following radial return procedure: given the stress deviator s and the equivalent plastic strain $\bar{\epsilon}^p$, we compute the stress measure

$$\bar{s} = \sqrt{3J2} = \sqrt{\frac{3}{2}(s : s)},$$

check if the yield condition is violated, i.e. $\bar{s} > Y(\bar{\epsilon}^p)$ and if so we update

$$s := \frac{\bar{s}^*}{\bar{s}} s \quad \text{and} \quad \bar{\epsilon}^p := \bar{\epsilon}^{p,*},$$

where \bar{s}^* and $\bar{\epsilon}^{p,*}$ solve the equations

$$\bar{s}^* = Y(\bar{\epsilon}^{p,*}) \quad \text{and} \quad 3\mu_s(\bar{\epsilon}^{p,*} - \bar{\epsilon}^p) = \bar{s} - \bar{s}^*.$$

We discretize the EPS, $\bar{\epsilon}^p$, using a finite element expansion in the thermodynamic basis $\{\phi_i\}$: $\bar{\epsilon}^p = \sum_k \bar{\epsilon}_k^p \phi_k$. This allows us to apply the above radial return algorithm independently to each of the degrees of freedom $(\mathbf{s}_{ij})_k$ and $\bar{\epsilon}_k^p$ of the deviatoric stress and EPS. If done in an appropriate basis (e.g. Bernstein polynomials) this can ensure that the matrix function s satisfies the constraint (12) at every point inside a zone. In practice, the approximation of the von Mises yield condition is good enough even when the rescaling is done in a more traditional Gauss-Legendre basis in which case (12) is only guaranteed at the Gauss-Legendre points in a zone.

The total stress is given by

$$\sigma = -pI + s + \sigma_a,$$

where σ_a is the stress due to artificial viscosity. The evaluation of this stress in the generalized force matrix integral of (26) is the main computational kernel of our method. Specifically, the matrix \mathbf{F} from (26) and the vector \mathbf{g} from (31) can be assembled from zonal contributions:

$$\mathbf{F} = \text{Assemble}(\mathbf{F}_z), \quad \mathbf{g} = \text{Assemble}(\mathbf{g}_z).$$

Note that the local rectangular force matrix \mathbf{F}_z is the high-order generalization of the “corner force” concept described in [22].

Evaluating \mathbf{F}_z and \mathbf{g}_z is a locally FLOP-intensive process based on transforming each zone back to the reference element where we apply a quadrature rule with points $\{\hat{q}_k\}$ and weights $\{\alpha_k\}$:

$$(\mathbf{F}_z)_{ij} \approx \sum_k \alpha_k \hat{\sigma}(\hat{q}_k) : \mathbf{J}_z^{-1}(\hat{q}_k) \hat{\nabla} \hat{w}_i(\hat{q}_k) \hat{\phi}_j(\hat{q}_k) |\det \mathbf{J}_z(\hat{q}_k)|,$$

$$(\mathbf{g}_z)_j \approx \sum_k \alpha_k \hat{\rho}(\hat{q}_k) \hat{g}(\hat{q}_k) \hat{\phi}_j(\hat{q}_k) |\det \mathbf{J}_z(\hat{q}_k)|,$$

where the “hat” symbol indicates definition with respect to the reference coordinate system. We aim to integrate (26) and (31) accurately using a quadrature rule of higher order compared to the degrees of freedom in the finite element spaces. For example, we use a 16-point Gaussian quadrature rule for the corner force computation for the 2D Q_2 - Q_1 method, where the velocity and internal energy have 18 and 4 degrees of freedom in each zone, respectively.

4.2. Fully-Discrete Formulation

Our fully discrete elastic-plastic formulation simply treats the semi-discrete equations from the previous section as a general system of non-linear ODEs, similar to [1].

Specifically, let $\mathcal{Y} = (\mathbf{v}, \mathbf{e}, \mathbf{s}, \mathbf{x})$. Then the semi-discrete equations can be written in the form:

$$\frac{d\mathcal{Y}}{dt} = \mathcal{F}(\mathcal{Y}, t),$$

where

$$\mathcal{F}(\mathcal{Y}, t) = \begin{pmatrix} \mathcal{F}_v(\mathbf{v}, \mathbf{e}, \mathbf{s}, \mathbf{x}) \\ \mathcal{F}_e(\mathbf{v}, \mathbf{e}, \mathbf{s}, \mathbf{x}) \\ \mathcal{F}_s(\mathbf{v}, \mathbf{e}, \mathbf{s}, \mathbf{x}) \\ \mathcal{F}_x(\mathbf{v}, \mathbf{e}, \mathbf{s}, \mathbf{x}) \end{pmatrix} = \begin{pmatrix} -\mathbf{M}_v^{-1} \mathbf{F} \cdot \mathbf{1} \\ \mathbf{M}_e^{-1} \mathbf{F}^T \cdot \mathbf{v} \\ \mathbf{M}_e^{-1} \mathbf{g} \\ \mathbf{v} \end{pmatrix}.$$

To solve the above system of ODEs, we use standard high order explicit Runge-Kutta time integration methods, where we incorporate the radial return procedure as a post-processing step after each Runge-Kutta stage. In the strong-stability preserving versions of the methods, e.g. RK3SSP, we can perform the rescaling on the Euler sub-step instead of the overall result from each stage.

4.3. The RK2-Average Scheme with Radial Return

As an example, we consider a modified two stage Runge-Kutta method which we refer to as the RK2-Average method. For the case of elastic-plastic flow, its two stages are given by

$$\begin{aligned}
\mathbf{v}^{n+\frac{1}{2}} &= \mathbf{v}^n - (\Delta t/2) \mathbf{M}_V^{-1} \mathbf{F}^n \cdot \mathbf{1} & \mathbf{v}^{n+1} &= \mathbf{v}^n - \Delta t \mathbf{M}_V^{-1} \mathbf{F}^{n+\frac{1}{2}} \cdot \mathbf{1} \\
\mathbf{e}^{n+\frac{1}{2}} &= \mathbf{e}^n + (\Delta t/2) \mathbf{M}_E^{-1} (\mathbf{F}^n)^T \cdot \mathbf{v}^{n+\frac{1}{2}} & \mathbf{e}^{n+1} &= \mathbf{e}^n + \Delta t \mathbf{M}_E^{-1} (\mathbf{F}^{n+\frac{1}{2}})^T \cdot \bar{\mathbf{v}}^{n+\frac{1}{2}} \\
\mathbf{s}^{n+\frac{1}{2}} &= \mathbf{s}^n + (\Delta t/2) \mathbf{M}_E^{-1} \mathbf{g}^n & \mathbf{s}^{n+1} &= \mathbf{s}^n + \Delta t \mathbf{M}_E^{-1} \mathbf{g}^{n+\frac{1}{2}} \\
\mathbf{s}^{n+\frac{1}{2}} &= \text{RadialReturn}(\mathbf{s}^{n+\frac{1}{2}}) & \mathbf{s}^{n+1} &= \text{RadialReturn}(\mathbf{s}^{n+1}) \\
\mathbf{x}^{n+\frac{1}{2}} &= \mathbf{x}^n + (\Delta t/2) \mathbf{v}^{n+\frac{1}{2}} & \mathbf{x}^{n+1} &= \mathbf{x}^n + \Delta t \bar{\mathbf{v}}^{n+\frac{1}{2}},
\end{aligned}$$

where $\mathbf{F}^k = \mathbf{F}(\mathcal{Y}^k)$, $\mathbf{g}^k = \mathbf{g}(\mathcal{Y}^k)$ and $\bar{\mathbf{v}}^{n+\frac{1}{2}} = (\mathbf{v}^n + \mathbf{v}^{n+1})/2$. To track the EPS in this case, we need one additional vector $\bar{\epsilon}^p$, which is updated only inside the `RadialReturn` procedure.

4.4. Axisymmetric Formulation

In this section we consider the modifications needed for problems where axial symmetry allows the reduction of a 3D simulation on $\Omega(t)$ to a computation in a 2D meridian cut $\Gamma(t)$.

Following [2], we introduce the axisymmetric mass matrices

$$(\mathbf{M}_V^{\mathbf{r}\mathbf{z}})_{ij} = \int_{\Gamma(t)} r \rho w_i w_j \quad \text{and} \quad (\mathbf{M}_E^{\mathbf{r}\mathbf{z}})_{ij} = \int_{\Gamma(t)} r \rho \phi_i \phi_j, \quad (33)$$

as well as the generalized *axisymmetric force matrix*

$$\mathbf{F}_{ij}^{\mathbf{r}\mathbf{z}} = \int_{\Gamma(t)} r (\sigma_{rz} : \nabla_{rz} w_i) \phi_j, \quad (34)$$

where we recall that in $z - r - \theta$ cylindrical coordinates

$$\nabla_{rz} v = \begin{pmatrix} \frac{\partial v_z}{\partial z} & \frac{\partial v_z}{\partial r} & 0 \\ \frac{\partial v_r}{\partial z} & \frac{\partial v_r}{\partial r} & 0 \\ 0 & 0 & \frac{v_r}{r} \end{pmatrix} = \begin{pmatrix} \nabla_{2d} v & 0 \\ 0 & \frac{v_r}{r} \end{pmatrix}, \quad \nabla_{rz} \cdot v = \frac{\partial v_z}{\partial z} + \frac{\partial v_r}{\partial r} + \frac{v_r}{r} = \nabla_{2d} \cdot v + \frac{v_r}{r},$$

and

$$\sigma_{rz} : \nabla_{rz} v = \sigma_{2d} : \nabla_{2d} v + \sigma_{\theta\theta} \frac{v_r}{r}.$$

Due to the axial symmetry, the stress deviator tensor has the form

$$s = \begin{pmatrix} s_{zz} & s_{zr} & 0 \\ s_{rz} & s_{rr} & 0 \\ 0 & 0 & s_{\theta\theta} \end{pmatrix}_{z-r-\theta} = \begin{pmatrix} s_{2d} & 0 \\ 0 & s_{\theta\theta} \end{pmatrix}$$

with $s_{zr} = s_{rz}$ and $s_{\theta\theta} = -(s_{zz} + s_{rr})$ since s is *symmetric* and *traceless*. The semi-discrete stress deviator rate equation then is

$$\frac{ds_{2d}}{dt} = g_{rz} \equiv \mu_s \left((\nabla_{2d} v + v \nabla_{2d}) - \frac{2}{3} (\nabla_{rz} \cdot v) I_{2d} \right) - \frac{s_{2d} (\nabla_{2d} v - v \nabla_{2d}) - (\nabla_{2d} v - v \nabla_{2d}) s_{2d}}{2}.$$

Note that we do not need to keep track of $s_{\theta\theta}$, since s is traceless and, in particular, the $J2$ invariant can be computed directly:

$$J2 = \frac{1}{2} \text{Tr}(s^2) = s_{zz}^2 + s_{zz}s_{rr} + s_{rr}^2 + s_{rz}^2.$$

Putting all of these together, we get the following semi-discrete approximation to the Euler equations in the axisymmetric case:

$$\text{Semi-Discrete Momentum Conservation: } \mathbf{M}_v^{\text{rz}} \frac{d\mathbf{v}}{dt} = -\mathbf{F}^{\text{rz}} \cdot \mathbf{1}, \quad (35)$$

$$\text{Semi-Discrete Energy Conservation: } \mathbf{M}_e^{\text{rz}} \frac{d\mathbf{e}}{dt} = (\mathbf{F}^{\text{rz}})^T \cdot \mathbf{v}, \quad (36)$$

$$\text{Semi-Discrete Stress Rate: } \mathbf{M}_e^{\text{rz}} \frac{d\mathbf{s}_{ij}}{dt} = \mathbf{g}_{ij}^{\text{rz}}, \quad (37)$$

$$\text{Semi-Discrete Equation of Motion: } \frac{d\mathbf{x}}{dt} = \mathbf{v}. \quad (38)$$

We have 3 unknown fields for the stress rate, s_{zz} , s_{rr} and s_{rz} , and the stress deviator rate is again based on a density-weighted projection, this time reduced to the meridian cut:

$$(\mathbf{g}_{ij}^{\text{rz}})_k = \int_{\Gamma(t)} r \rho (g_{rz})_{ij} \phi_k.$$

As in the Cartesian case, we apply radial return to the degrees of freedom of s after the computation in (37).

5. Numerical Results

We now present a series of numerical results using various high-order methods corresponding to specific choices for the finite element spaces describing the kinematic variables of position x and velocity v , and the thermodynamic variables e and s . We designate each method using the notation Q_k - Q_{k-1} (for quadrilateral / hexahedral meshes) as described in [1]. We consider both traditional h -refinement (or mesh refinement) as well as p -refinement where we keep the mesh fixed while increasing the order of the method.

For all test cases considered, we solve the global linear system for momentum conservation using a diagonally scaled conjugate gradient algorithm to a residual tolerance of 10^{-10} and we use the type 4 artificial viscosity from [1]. Unless otherwise specified, we use artificial viscosity coefficients $q_1 = 1/10$ and $q_2 = 2$. Unless explicitly given, all physical units in this section are based on the $(cm, g, \mu s)$ unit system, which means velocities are in $\frac{cm}{\mu s}$, densities are in $\frac{g}{cm^3}$ and stresses are in $Mbar$. In most cases, we make use of a Grüneisen equation of state of the form

$$p(\mu, e) = \frac{\rho_0 C_0^2 \mu \left(1 + \left(1 - \frac{\gamma_0}{2}\right) \mu - \frac{b}{2} \mu^2\right)}{1 - (S_1 - 1) \mu} + (\gamma_0 + b \mu) \rho_0 e; \quad \mu \equiv \frac{\rho}{\rho_0} - 1, \quad (39)$$

see [23] for further details. The results in this section have been computed with our high-order finite element hydrocode BLAST [24], which is based on the parallel modular finite element methods library MFEM [25].

5.1. Elastic Wave Propagation with Non-Linear EOS

In this simple test problem, we consider the 1D propagation of an elastic wave in a material characterized by a non-linear equation of state. In particular, the EOS has the form

$$p(\mu, e) = \mu + \mu^2 + \mu^3 + (1 + \mu + \mu^2) \frac{e}{\rho_0}; \quad \mu \equiv \frac{\rho}{\rho_0} - 1.$$

The goal of this problem is to verify the order of accuracy for the time integration of the semi-discrete stress rate evolution equation (as well as the other semi-discrete conservation laws) and was originally developed by [26]. The computational domain is a simple 1D mesh with $x \in [0, 1]$, and $\Delta x = 1/16$. The mesh has finite dimension in y , with $y \in [0, 0.1]$ and $\Delta y = 1/10$ (a single zone in y). The mesh is filled with a material with $\rho_0 = 1$ and $e_0 = 0$. The material has a shear modulus $\mu_s = 1$, and an effectively “infinite” yield stress $Y = 10^{10}$ to eliminate plasticity effects. The x -component of the velocity is initialized with

$$v_x = 0.01 \sin(\pi x).$$

The diagnostic is the value of the x -component of the velocity at a Lagrangian “tracer” point in the mesh with an initial location of $x = 1/4$, at a final time of $t = 0.3$. Since this problem is smooth we run without any artificial viscosity. We perform a sequence of 4 calculations with fixed time steps of $\Delta t = 1/400, 1/800, 1/1600$ and $1/3200$ using a Q_2 - Q_1 spatial discretization. The temporal error of the diagnostic is measured for each calculation at the final time $t = 0.3$ with respect to a reference calculation performed with a time step of $\Delta t = 1/12800$. We are therefore checking the *self-convergence* of our methods.

The results of this test are summarized in Table 1 and plotted in Figure 1. For each time integration method, we achieve the theoretical rates of first, second, third and fourth order error convergence in time, even for the case of a non-linear EOS. We point out that this is only possible by evaluating the hydrodynamic state variables (including the EOS and the stress rate) at *each step* of the multi-stage time integrator. To our knowledge, there is no method which can achieve 2nd order (or greater) convergence on this test that does not evaluate the EOS and stress rate at each sub-stage of the time integration.

Table 1: Temporal errors $|v_x - v_x^{ref}|$ for Lagrangian tracer point at a final time of $t = 0.3$ for the 1D elastic wave test problem using a sequence of fixed time steps and four different explicit time integration methods.

Method	$\Delta t = 1/400$	$\Delta t = 1/800$	$\Delta t = 1/1600$	$\Delta t = 1/3200$
Order 1: EulerAvg	2.1125e-04	8.6947e-06	4.3328e-06	2.1656e-06
Order 2: RK2Avg	2.2392e-07	5.4413e-08	1.3434e-08	3.3391e-09
Order 3: RK3SSP	1.4639e-08	1.6607e-09	1.9519e-10	2.3660e-11
Order 4: RK4	8.1659e-10	4.9890e-11	3.0400e-12	1.8000e-13

5.2. Bazan Elastic-Plastic Shock Wave

Here we consider a 1D flyer impact problem which generates an elastic-plastic shock wave; a two shock state with an elastic precursor shock followed by a plastic shock. The analytic solution to this test problem was developed by [27]. The problem geometry is a 2D (r, z)

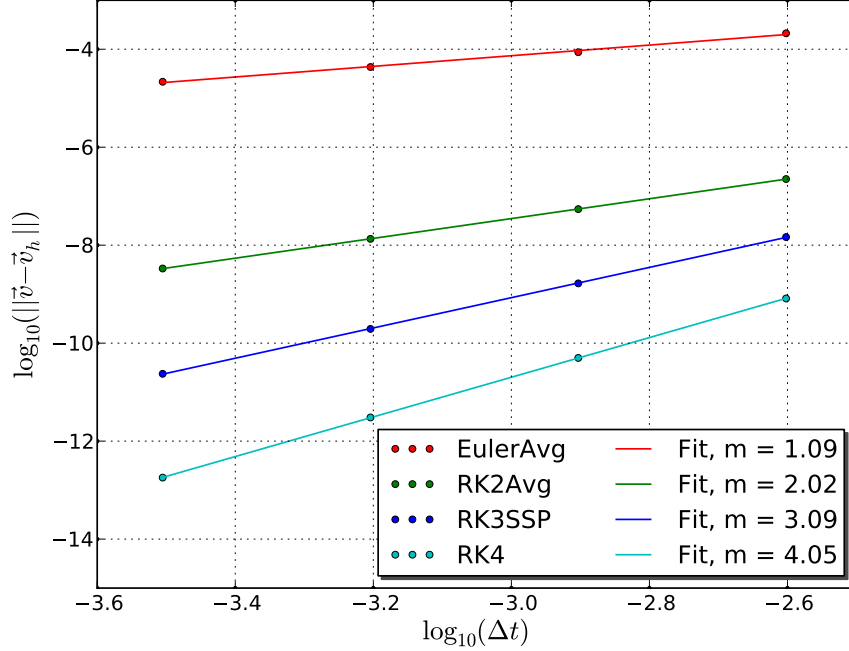


Figure 1: Error convergence in time for simple 1D elastic wave test problem using four different time integration methods.

cylindrical domain with $r \in [0, 0.1]$ and $z \in [0, 1]$. The domain consists of two pieces of a vanadium like material, separated by a contact at $z = 0.5$. The initial conditions for the left and right sates are:

$$v_z = \begin{cases} 0.060281 & z \leq 0.5 \\ 0 & z > 0.5 \end{cases}, \quad \rho = \begin{cases} 6.1 & z \leq 0.5 \\ 6.1 & z > 0.5 \end{cases}, \quad e = \begin{cases} 0 & z \leq 0.5 \\ 0 & z > 0.5 \end{cases}.$$

The material has a shear modulus $\mu_s = 0.481$, a yield stress $Y = 0.025$ and obeys a simplified form of the Grüneisen EOS of (39) with coefficients $C_0 = 0.5077$, $S_1 = 1.201$ and all other coefficients with zero value. We run the problem to a final time of $t = 0.5$. In each case below, we use the energy conserving RK2-Average time integrator.

5.2.1. 1D Results

Here we compare results on a 1D mesh consisting of a single zone in the radial direction. We consider a testing matrix based on h - and p -refinement of the problem as shown in Table 2 and focus on three cases:

1. A fixed number of spatial degrees of freedom for each case.
2. h -refinement using the Q_2 - Q_1 spatial method.
3. p -refinement using the $\Delta x = 1/200$ mesh.

In Figure 2 we compare results for the velocity, density and the components of the stress deviator tensor using two different high order methods, each with an identical number of kinematic and thermodynamic degrees of freedom. This is accomplished by de-refining the mesh one level for every doubling of the order of the kinematic space. When plotting high-order field data, sub-zonal sampling of the solution is critical for capturing the sub-zonal

Table 2: Summary of h - and p -refinement cases for the 1D elastic-plastic shock wave problem.

Spatial Order	Base Mesh	1st Refinement	2nd Refinement
Q_2 - Q_1	$\Delta x = 1/200$	$\Delta x = 1/400$	$\Delta x = 1/800$
Q_4 - Q_3	$\Delta x = 1/200$	–	–
Q_8 - Q_7	$\Delta x = 1/200$	–	–

resolution of the fields. For our baseline Q_2 - Q_1 method, we sample the field at 4 points per zone (in one dimension) and we double this number for every doubling of the spatial approximation order. The stress deviator components do not exceed their threshold values due to the radial return process, but we do observe spurious behavior at the material contact due to the wall heating effect. Furthermore, the low order method on the fine mesh yields essentially the same result as the high-order method on the coarse mesh.

In Figure 3 and Figure 4 we show zoomed in views of the velocity and density fields around one of the shocks and compare results for both h -refinement (keeping the approximation order fixed and doubling the mesh resolution) and p -refinement (keeping the mesh fixed and doubling the approximation order). For both h - and p -refinement strategies, we observe convergence to the exact solution, see Figure 5. Both refinement strategies give virtually identical errors for the same number of degrees of freedom, e.g. ($h = 1/800$, $p = 2$) vs ($h = 1/200$, $p = 8$) due to the discontinuous nature of the analytic solution. While higher-order methods (p -refinement) do not provide an accuracy advantage for discontinuous solutions in this case, we will demonstrate their superiority in symmetry preservation in Section 5.3.1.

5.2.2. 2D (r, z) Results on Unstructured Mesh

In this section we discuss the results from the axisymmetric formulation on a 2D, highly unstructured mesh. In Figure 6 we compare results for the velocity, density and the components of the stress deviator tensor using two different high order methods, each with an identical number of kinematic and thermodynamic degrees of freedom. For 2D meshes, we sample the fields at 16 points per zone for the Q_2 - Q_1 method and 64 points per zone for the Q_4 - Q_3 method. Note the degree to which the 1D symmetry of the velocity and density is preserved in both cases, even on the unstructured 2D mesh. In this case, we observe that the stress deviator components do exceed their threshold values and the spurious behavior at the material contact due to the wall heating effect is more pronounced, although the effect is diminished for the Q_4 - Q_3 method. In Figure 7 we show pseudocolor plots of the density field along with the computational mesh, zoomed in around one of the shocks. Note the sub-zonal resolution of both the elastic precursor and plastic shock waves on the unstructured 2D mesh.

5.3. Spherical Shell Collapse

In this test problem we consider the collapse of a spherical shell of beryllium given an initial inwardly directed radial velocity profile. The initial kinetic energy of the shell is converted to internal energy via plastic work as the shell collapses. During this process, the shell thickens and eventually stops once the initial kinetic energy has been completely

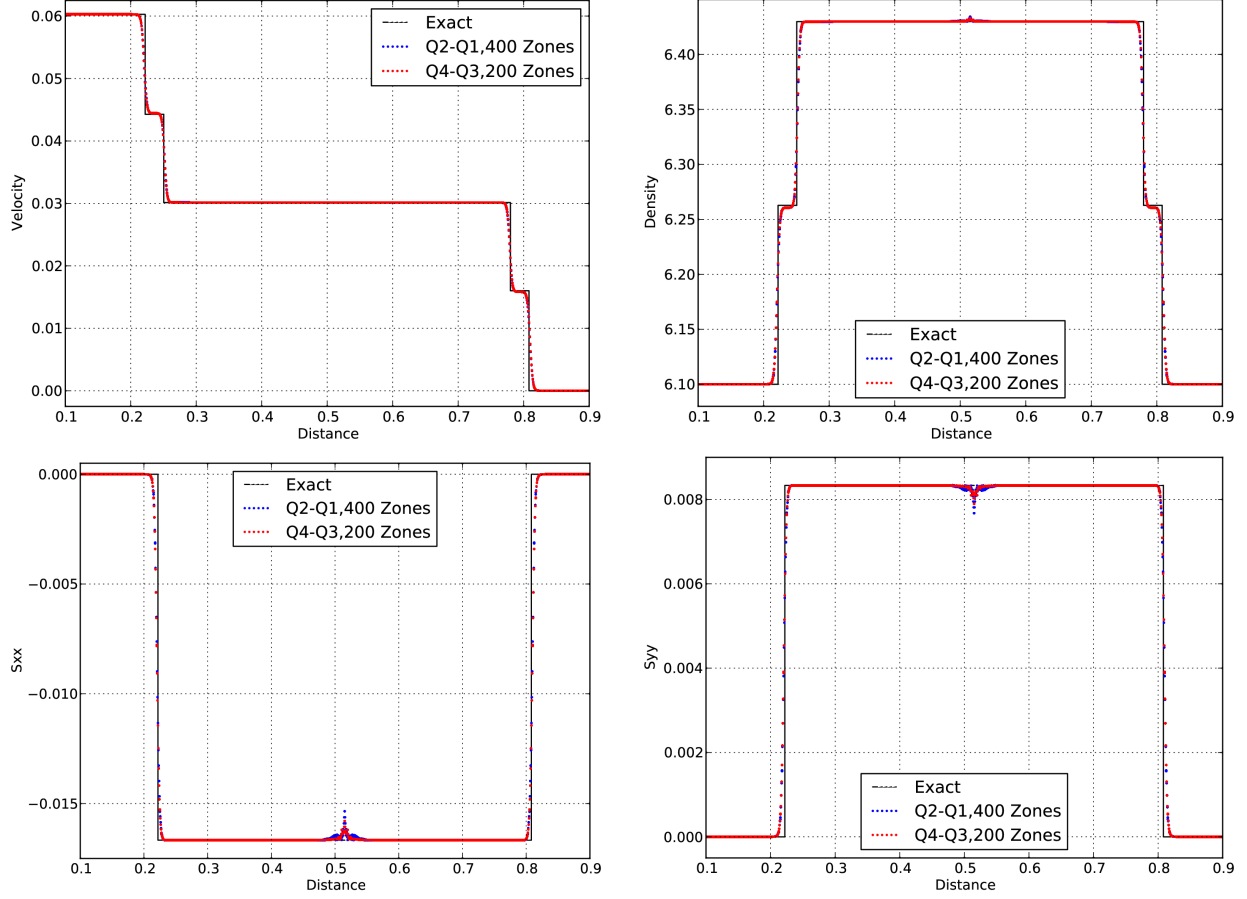


Figure 2: Scatter plots of velocity (*top-left*), density (*top-right*) and stress deviator components (*bottom*) versus distance for the 1D elastic-plastic shock wave problem using a Q_2 - Q_1 method on a 400 zone mesh with 4 plot points per zone and a Q_4 - Q_3 method on a 200 zone mesh with 8 plot points per zone.

dissipated. The analytic values for the inner and outer stopping radii of the shell have been developed for the case of 1D cylindrical and spherical symmetries, assuming incompressible, elastic, perfectly plastic flow [28, 15, 29].

We consider a spherical shell with an inner radius of 8 and a thickness of 2. We use the Grüneisen EOS of (39) with coefficients $C_0 = 1.287, S_1 = 1.124, \gamma_0 = 1.11, \rho_0 = 1.84$ and all other coefficients with zero value. We use an elastic, perfectly plastic strength model with a shear modulus $\mu_s = 1.51$ and a yield stress $Y = 0.0033$. The velocity of the shell is initialized as

$$v(r) = -v_0 \left(\frac{R_i}{r} \right)^2 \hat{r},$$

where R_i is the initial inner radius of the shell and \hat{r} is a unit radial vector. The initial velocity magnitude is chosen as $v_0 = 0.0675306$ which gives a final outer stopping radius $r_o = 8.0156$ and a final inner stopping radius of $r_i = 3.0$ as shown in [29, 13]. We run the problem to a final time of $t = 102$, and in this example, we use a value of $q_1 = 1/20$ for the artificial viscosity. In each case below, we use the energy conserving RK2-Average time integrator. As stated in [15], the figures of merit for numerical solutions to this problem are (i) the

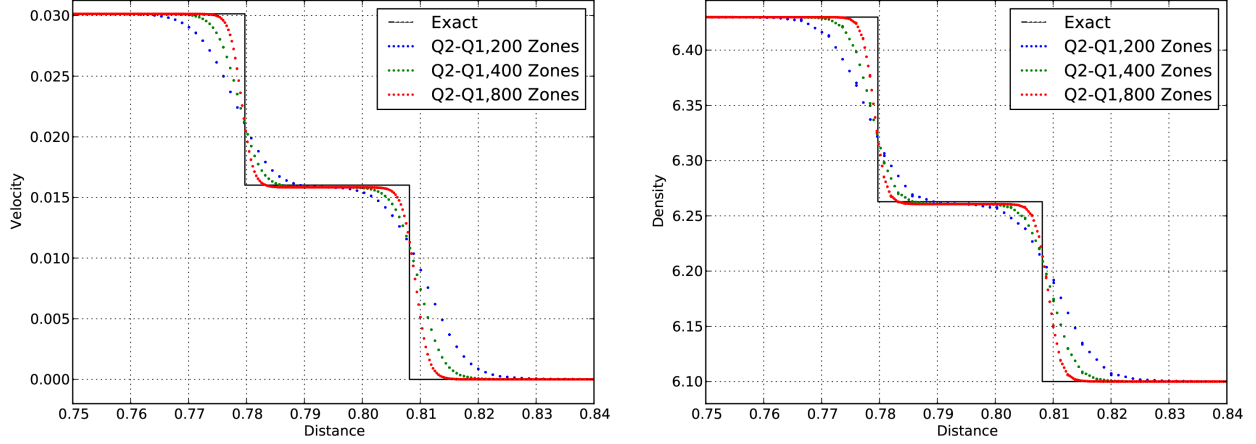


Figure 3: Scatter plots of velocity (*left*) and density (*right*) versus distance zoomed in around one of the shocks, using a Q_2 - Q_1 method with h -refinement and 4 plot points per zone.

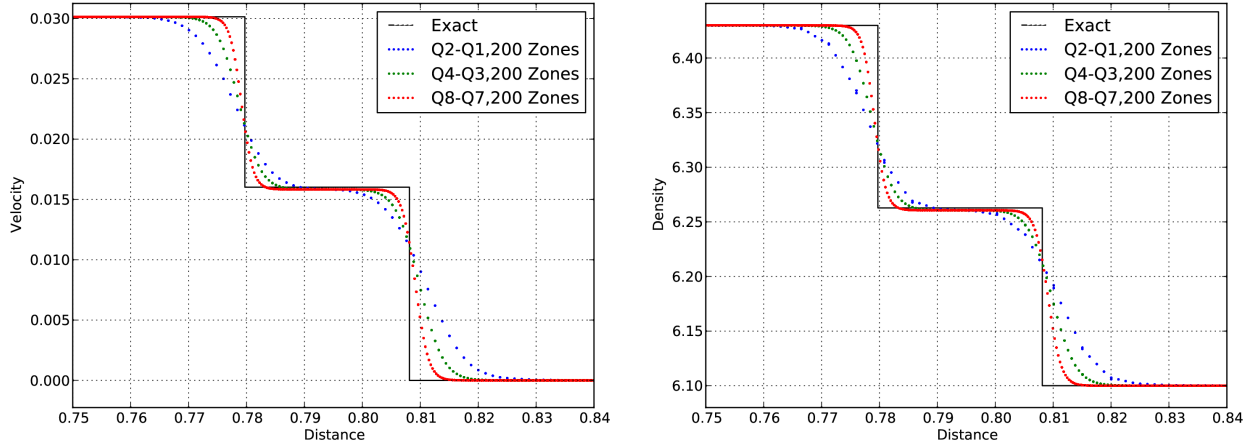


Figure 4: Scatter plots of velocity (*left*) and density (*right*) versus distance zoomed in around one of the shocks, using a 200 zone mesh with p -refinement and 4, 8 and 16 plot points per zone.

method accurately predicts the inner and outer stopping radii and (ii) the computational mesh maintains spherical symmetry.

5.3.1. 2D (r, z) Results: p -Refinement on Smoothly Perturbed Mesh

First, we consider a 2D (r, z) axisymmetric version of this problem. To emphasize the symmetry preserving benefits of high order methods, we apply a smooth perturbation to the computational mesh to break its radial symmetry. The perturbation is first applied to the y -coordinates of a 16 by 16 mesh of the unit square of the form:

$$\Delta y = 0.1 \cos(6\pi x),$$

$$y = \begin{cases} y + 2y\Delta y, & y < 0.5 \\ y + 2(1 - y)\Delta y, & y \geq 0.5 \end{cases}.$$

The perturbed unit square is then mapped to an annulus with the specified inner and outer radii as depicted in Figure 8.

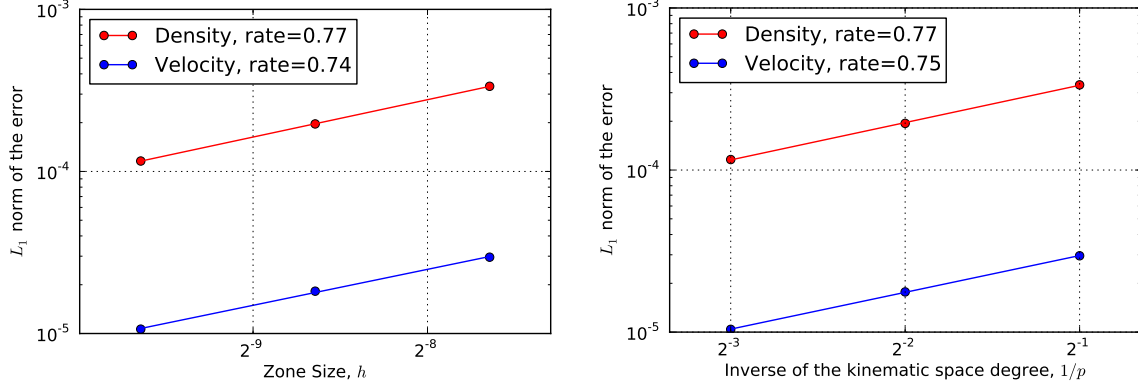


Figure 5: Convergence rates for the 1D elastic-plastic shock wave problem using h -refinement (left) and p -refinement (right).

We consider p -refinement on the perturbed 2D mesh, using a sequence of successively higher order methods. In Figure 9, we show pseudocolor plots of the internal energy field and the curvilinear mesh at the final stopping time of $t = 102$ using Q_2 - Q_1 , Q_4 - Q_3 and Q_8 - Q_7 methods with 16, 64 and 256 plot points per zone respectively. Note the curvature of the meshes as well as the sub-zonal resolution of the internal energy field. For the lowest order method, the inner radius has noticeable symmetry breaking, while the higher order methods do not break symmetry (this is further quantified in Figure 11 and Figure 12).

In Figure 10 we plot the total, kinetic and internal energies of the problem for each method. For each calculation, the total energy was conserved to machine precision via the energy conserving RK2-Average time integration method. As the order of the method is increased, we observe convergence in the evolution of the kinetic and internal energies as the initial kinetic energy is completely dissipated via plastic work at the final stopping time. In Figure 11 we plot the average values of the inner and outer radii as a function of time and compare the calculated stopping radii to the analytic values. As the order of the method is increased, the average outer and inner radial values converge to the analytic values at the final stopping time, as seen in Figure 12. In Figure 11 we also plot the normalized standard deviation of the radial surfaces which indicates the percent symmetry error over time. The symmetry error in both the outer and inner radial interfaces decreases substantially under p -refinement (see Figure 12) and the final symmetry error for the inner radius is less than 10^{-5} percent for the Q_8 - Q_7 method on the initially perturbed mesh. Contrast the convergence rate for p -refinement with that of h -refinement as shown in the next section.

5.3.2. 3D Results: h -Refinement on Unstructured Mesh

Here we consider a full 3D treatment of the problem. In this case we compare results obtained using a Q_2 - Q_1 method on a sequence of refined 3D unstructured meshes to verify spatial convergence with respect to mesh refinement. In Figure 13, we show pseudocolor plots of the internal energy field and the curvilinear mesh at the final stopping time of $t = 102$ on a very coarse unstructured mesh with 4 angular zones in the θ and ϕ directions and 8 radial zones, as well as two uniformly refined version of the same mesh. For these 3D examples, we sample the solutions using a lattice of 4^3 points for each zone. Note the spherical curvature

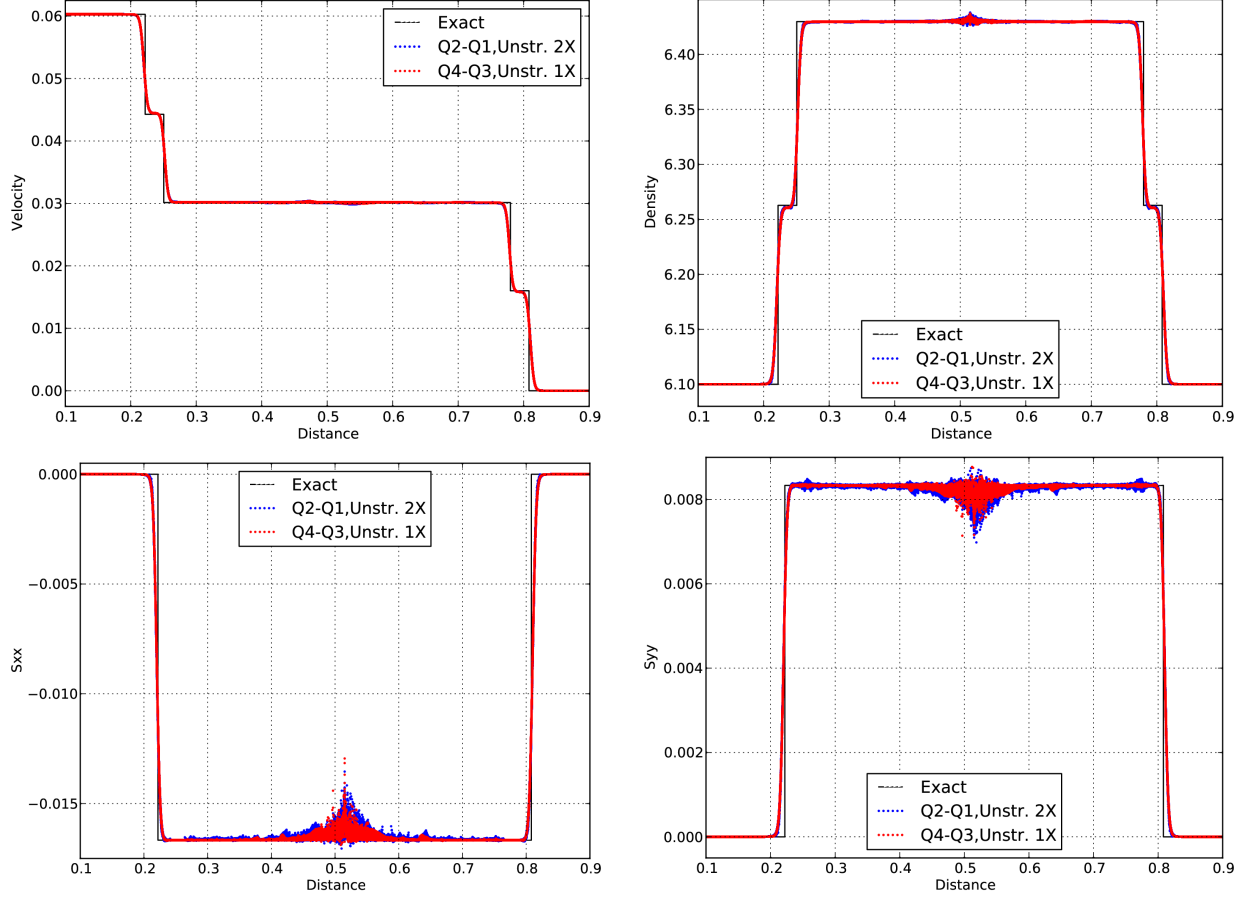


Figure 6: Scatter plots of velocity (*top-left*), density (*top-right*) and stress deviator components (*bottom*) versus distance for the 2D (r, z) elastic-plastic shock wave problem using a Q_2-Q_1 method on a refined unstructured mesh with 16 plot points per zone and a Q_4-Q_3 method on a coarse unstructured mesh with 64 plot points per zone.

of the radial interfaces, even on the coarsest mesh.

In Figure 14 we plot the total, kinetic and internal energies of the problem for each mesh. Again, for each calculation, the total energy was conserved to machine precision. As the mesh is refined, we observe convergence in the evolution of the kinetic and internal energies as the initial kinetic energy is completely dissipated via plastic work at the final stopping time. In Figure 15 we plot the average values of the inner and outer radii as a function of time and compare the calculated stopping radii to the analytic values. As the mesh is refined, the average outer and inner radial values converge to the analytic values at the final stopping time. In Figure 15 we also plot the normalized standard deviation of the radial surfaces which indicates the symmetry error over time. Here we are sampling the symmetry error at 16 points per face. The symmetry error in both the outer and inner radial interfaces is decreasing under mesh refinement as shown in Figure 16, however, the rate is substantially less for traditional h -refinement when compared to the p -refinement results of Section 5.3.1.

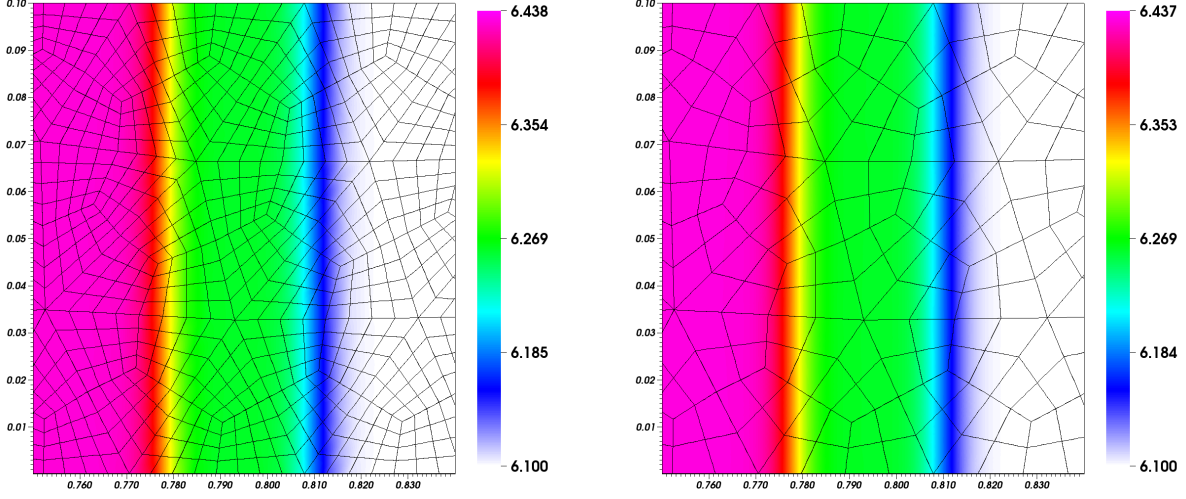


Figure 7: Pseudocolor plots of density and mesh for the 2D (r, z) elastic-plastic shock wave problem, zoomed in around one of the shocks, using a Q_2 - Q_1 method on a refined unstructured mesh with 16 plot points per zone (*left*) and a Q_4 - Q_3 method on a coarse unstructured mesh with 64 plot points per zone (*right*).

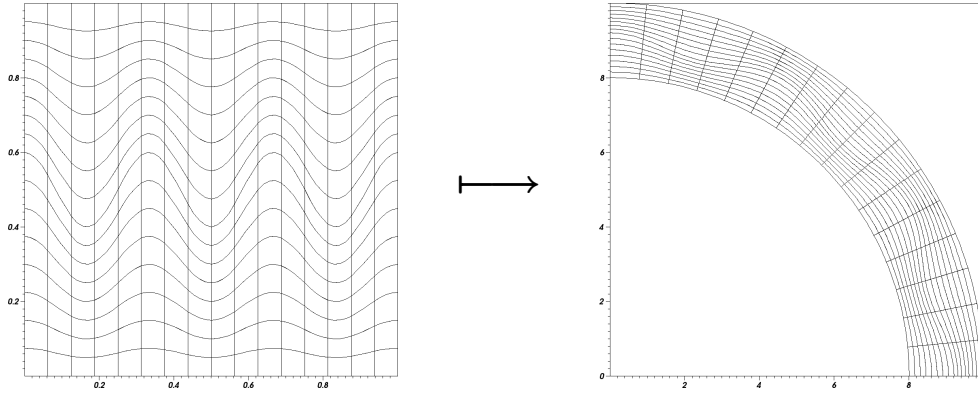


Figure 8: A smoothly perturbed 16 by 16 Q_2 mesh of the unit square is transformed to an annulus.

5.4. High Velocity Impact Problems

Here we consider two different problems where a metal projectile impacts a rigid wall at high velocity resulting in significant plastic deformation and Lagrangian mesh motion.

5.4.1. 2D Planar Impact

First, we consider a simple 2D planar impact of an aluminum projectile against a rigid wall, as described in [17, 10]. The initial projectile is a rectangular plate of length $l = 500$ and thickness $h = 100$. We use the Grüneisen EOS from (39) for the aluminum with $\rho_0 = 2.785$, $C_0 = 0.5328$, $S_1 = 1.338$, $\gamma_0 = 2.0$ and all other coefficients with zero value. We use an elastic, perfectly plastic strength model with a shear modulus $\mu_s = 0.276$ and a yield stress $Y = 0.003$. The velocity of the projectile is initialized in the negative x -direction with a magnitude of 0.015. In this example, we use a Q_4 - Q_3 method on a sequence of refined 2D meshes of the domain $[0, 500] \times [-50, 50]$. In Figure 17 we plot the plasticity threshold map (defined as $\sqrt{\frac{3}{2}(s:s)/Y}$), an indicator of where the material has exceeded the plastic

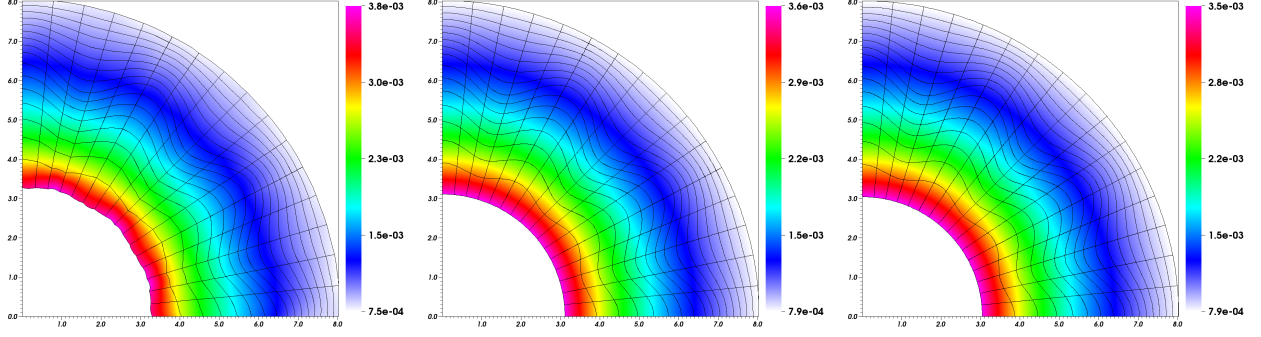


Figure 9: Pseudocolor plots of internal energy and curvilinear mesh for the 2D (r, z) spherical shell collapse problem, on a smoothly perturbed 16 by 16 2D mesh sing using a Q_2 - Q_1 , Q_4 - Q_3 and a Q_8 - Q_7 method (*left to right*) with 16, 64 and 256 plot points per zone respectively.

yield limit, for the medium resolution mesh. In Figure 18 we plot the total, kinetic and internal energies of the problem for each mesh. As with previous examples, the plots suggest convergence in the evolution of the kinetic and internal energies as the initial kinetic energy is completely dissipated via plastic work.

5.4.2. 3D Taylor Impact

Finally, we consider a 3D impact of a cylindrical copper rod against a rigid wall, as described in [16, 14]. The initial projectile is a cylindrical rod of length $l = 3.24$ and radius $r = 0.32$. We use the Grüneisen EOS of (39) for the copper with coefficients $C_0 = 0.361966$, $S_1 = 1.489$, $\gamma_0 = 2.02$, $b = 0.47$, and $\rho_0 = 8.93$. We use an elastic, linearly plastic strength model with a shear modulus $\mu_s = 0.43333$, initial yield stress of $Y_0 = 0.004$ and a linear work hardening modulus $Y_{wh} = 0.001$, i.e. $Y(\bar{\epsilon}^p) = Y_0 + Y_{wh}\bar{\epsilon}^p$. The velocity of the projectile is initialized in the positive x -direction with a magnitude of 0.0227. In this example, we use both a 2D (r, z) Q_4 - Q_3 method and a full 3D Q_4 - Q_3 method on an unstructured, curvilinear cylindrical mesh. Using Q_4 - Q_3 finite elements gives 25 kinematic degrees of freedom per zone for the 2D case and 125 kinematic degrees of freedom per zone for the 3D case. In Figure 19 we plot the equivalent plastic strain and curvilinear meshes for both the 2D (r, z) and 3D methods. In Figure 20 we plot the total, kinetic and internal energies of the problem for each mesh, where for both cases, total energy was conserved to machine precision. The agreement between the 2D (r, z) and 3D calculations, summarized in Table 3, is very good and can be compared to the results from [16, 14, 30].

Table 3: Summary of final results at time $t = 80$ for the Taylor impact problem using 2D (r, z) and full 3D Q_4 - Q_3 methods.

Method	Final Length	Max. Radius	Max. EPS	50% Kinetic Energy Time
2D (r, z)	2.1738	0.6742	4.20	25.102
3D	2.1739	0.6741	4.19	25.099

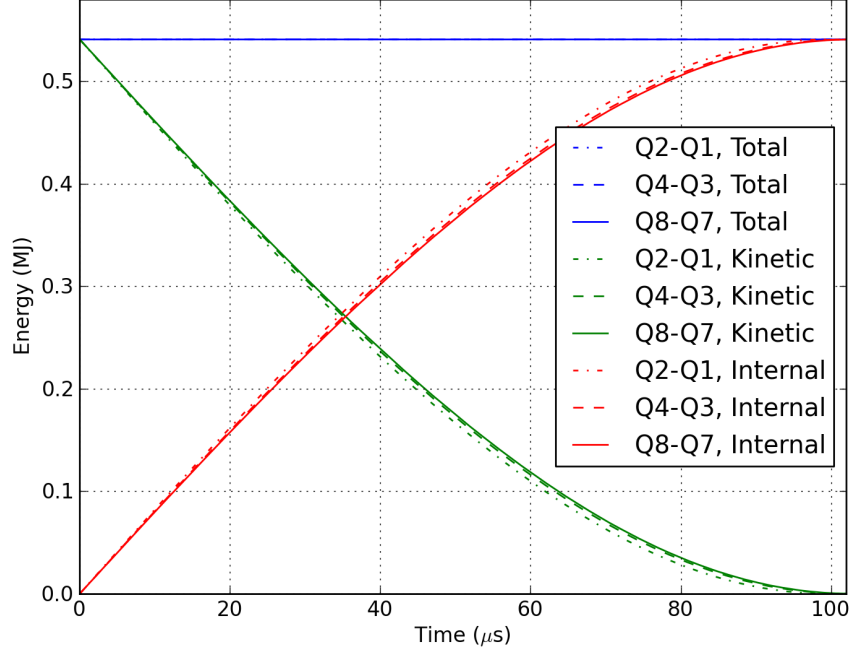


Figure 10: Total, kinetic and internal energies vs. time for the 2D (r, z) spherical shell collapse problem on a smoothly perturbed 16 by 16 2D mesh with p -refinement.

6. Conclusions

We have presented an extension of our high-order curvilinear finite element method for solving the equations of compressible hydrodynamics in a Lagrangian frame to the case of elastic-plastic material dynamics. This was achieved by augmenting the semi-discrete conservation equations with an additional equation for the deviatoric stress which is discretized using a density weighted L_2 projection on the thermodynamic basis. The fully discrete conservation laws, including the stress deviator evolution equation, are solved using explicit high-order Runge-Kutta methods and radial return is applied to the deviatoric stress degrees of freedom at each sub-stage. We demonstrated convergence of our method using both h - and p -refinement strategies on multiple test problems. We also demonstrated via numerical examples the benefits of using high order curvilinear finite elements in this context, including: improved symmetry preservation for non-uniform and unstructured meshes, the ability to more accurately capture the geometry of the flow and maintain robustness with respect to mesh motion using curvilinear zones and sharper resolution of a shock front for a given mesh resolution including the ability to resolve both elastic and plastic shocks at the sub-zone level.

Acknowledgments

The authors would like to acknowledge P-H. Maire, R. Abgrall, J. Breil, R. Loubere and B. Rebouret for sharing their work [10] which was very influential in the development of this paper.

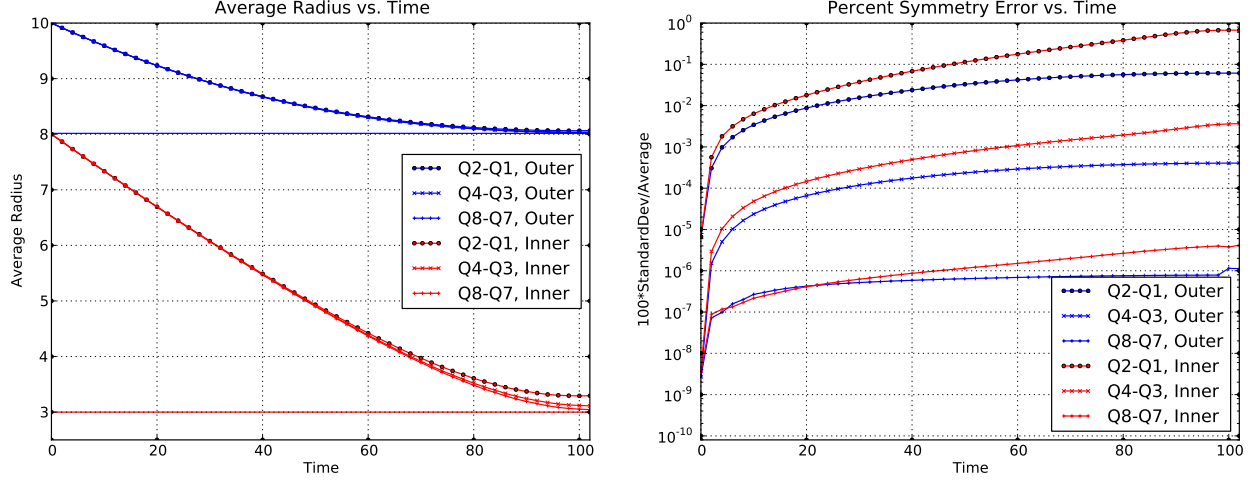


Figure 11: Average interface radii vs. time (*left*) and percent symmetry errors vs. time (*right*) for the 2D (r, z) spherical shell collapse problem on a smoothly perturbed 16 by 16 2D mesh with p -refinement.

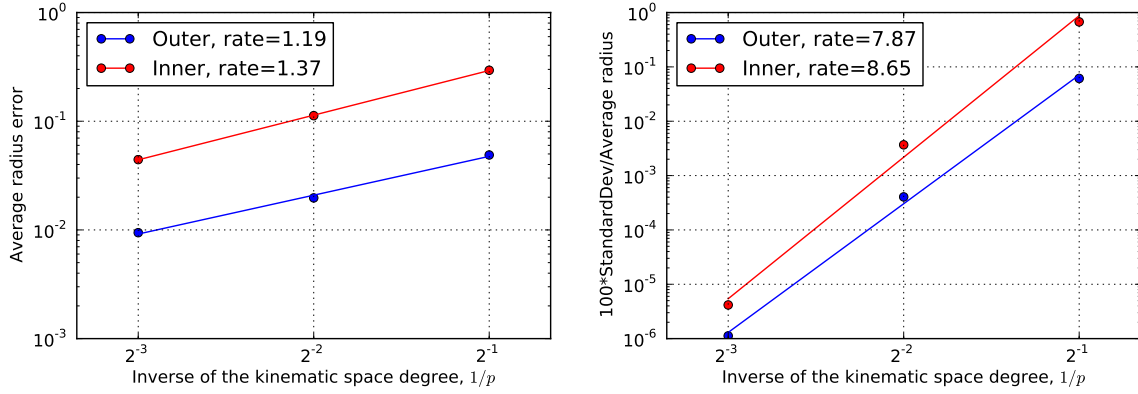


Figure 12: Convergence rates for the average radii (*left*) and percent symmetry errors (*right*) at the final time for the 2D (r, z) spherical shell collapse problem on a smoothly perturbed 16 by 16 2D mesh with p -refinement.

References

- [1] V. A. Dobrev, Tz. V. Kolev, and R. N. Rieben. High order curvilinear finite element methods for Lagrangian hydrodynamics. *SIAM J. Sci. Comp.*, 34(5):B606–B641, 2012. Also available as LLNL technical report LLNL-JRNL-516394.
- [2] V. A. Dobrev, T. E. Ellis, Tz. V. Kolev, and R. N. Rieben. High order curvilinear finite elements for axisymmetric Lagrangian hydrodynamics. *Computers and Fluids*, 2012. in press, <http://dx.doi.org/10.1016/j.compfluid.2012.06.004>.
- [3] M. L. Wilkins. *Methods in Computational Physics*, volume 3, chapter Calculation of Elastic-Plastic Flow. Academic Press, 1964.
- [4] J. T. Cherry, S. Sack, G. Maenchen, and V. Kransky. Two-dimensional stress-induced

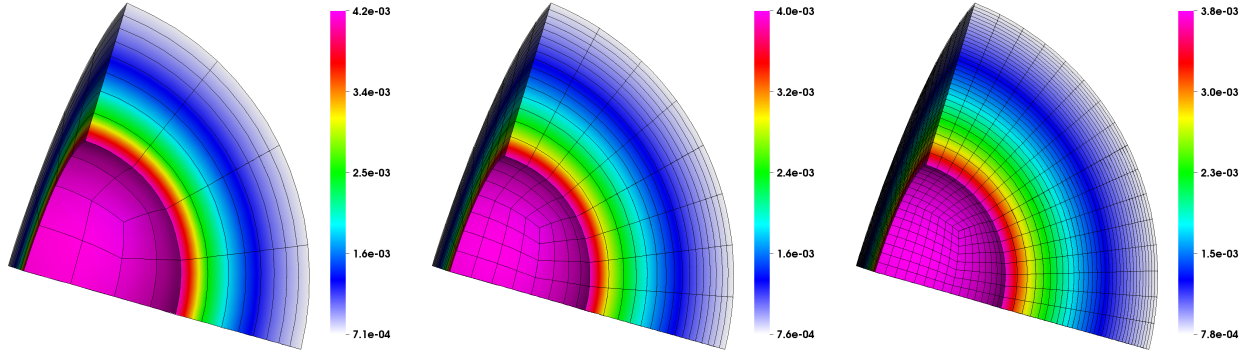


Figure 13: Pseudocolor plots of internal energy and curvilinear mesh for the 3D spherical shell collapse problem, using a Q_2 - Q_1 method on a sequence of refined meshes with 64 plot points per zone.

adiabatic flow. Technical Report UCRL-50987, Lawrence Livermore National Laboratory, 1970.

- [5] V. A. Dobrev, T. E. Ellis, Tz. V. Kolev, and R. N. Rieben. Curvilinear finite elements for Lagrangian hydrodynamics. *Internat. J. Numer. Methods Fluids*, 65(11-12):1295–1310, 2010.
- [6] H. Ockendon and J. Ockendon. *Waves and Compressible Flow*, volume 47 of *Texts in Applied Mathematics*. Springer-Verlag, 2004.
- [7] D. J. Benson. Computational methods in Lagrangian and Eulerian hydrocodes. *Comput. Methods Appl. Mech. Engrg.*, 99:235–394, 1992.
- [8] A. J. M. Spencer. *Continuum Mechanics*. Dover Publications Inc., Mineola, New York, 1980.
- [9] J. C. Simo and T. J. R. Hughes. *Computational Inelasticity*. Springer, 1998.
- [10] P-H. Maire, R. Abgrall, J. Breil, R. Loubère, and B. Rebouret. A nominally second-order cell-centered Lagrangian scheme for simulating elastic-plastic flows on two-dimensional unstructured grids. *J. Comput. Phys.*, 2012. <http://dx.doi.org/10.1016/j.jcp.2012.10.017>.
- [11] G. Maenchen and S. Sack. *Methods in Computational Physics*, volume 3, chapter The TENSOR Code. Academic Press, 1964.
- [12] S. K. Sambasivan, M. J. Shashkov, and D. E. Burton. Exploration of new limiter schemes for stress tensors in Lagrangian and ALE hydrocodes. *Computers and Fluids*, 2012. <http://dx.doi.org/10.1016/j.compfluid.2012.04.010>.
- [13] M. A. Kelmanson and S. B. Maunders. Modeling high-velocity impact phenomena using unstructured dynamically adaptive Eulerian meshes. *Comput. Methods Appl. Mech. Engrg.*, 142:269–301, 1997.

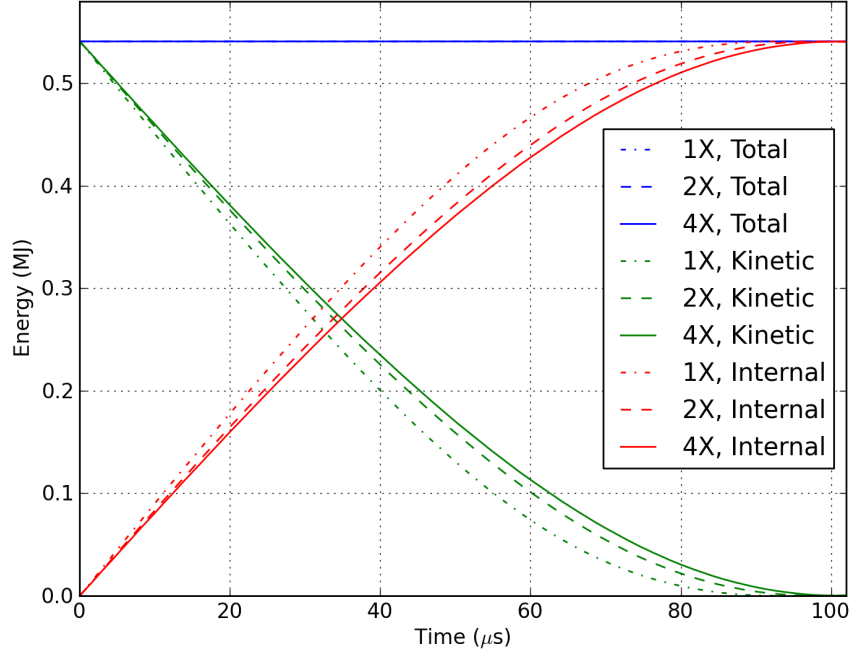


Figure 14: Total, kinetic and internal energies vs. time for the 3D spherical shell collapse problem using a Q_2 - Q_1 method on a sequence of refined meshes.

- [14] H.S. Udaykumar, L. Tran, D. M. Belk, and K.J. Vanden. An Eulerian method for computation of multimaterial impact with ENO shock-capturing and sharp interfaces. *J. Comput. Phys.*, 186(1):136–177, 2003.
- [15] B. P. Howell and G. J. Ball. A free-Lagrange augmented Godunov method for the simulation of elastic-plastic solids. *J. Comput. Phys.*, 175:128–167, 2002.
- [16] G. T. Camacho and M. Ortiz. Adaptive Lagrangian modeling of ballistic penetration of metallic targets. *Comput. Methods Appl. Mech. Engrg.*, 142:269–301, 1997.
- [17] G. Kluth and B. Despres. Discretization of hyperelasticity on unstructured mesh with a cell-centered Lagrangian scheme. *J. Comput. Phys.*, 229(24):9092–9118, 2010.
- [18] L. D. Landau and E. M. Lifshitz. *Theory of Elasticity, 3rd Ed.* Pergamon Press, 1986.
- [19] M. L. Wilkins. Calculation of Elastic-Plastic Flow. Technical Report UCRL-7322, Rev. 1, Lawrence Livermore National Laboratory, 1969.
- [20] R. Tipton. CALE Lagrange step. Technical report, Lawrence Livermore National Laboratory, October 1990. Unpublished.
- [21] J. K. Dienes. On the analysis of rotation and stress rate in deforming bodies. *Acta Mechanica*, 32:217–232, 1978.
- [22] E. J. Caramana, D. E. Burton, M. J. Shashkov, and P. P. Whalen. The construction of compatible hydrodynamics algorithms utilizing conservation of total energy. *J. Comput. Phys.*, 146:227–262, 1998.

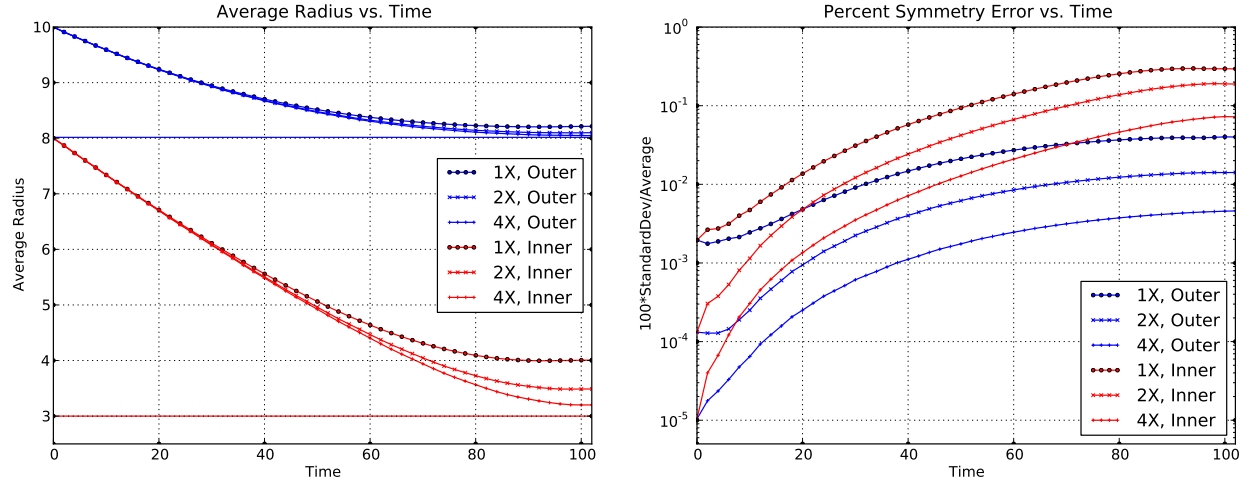


Figure 15: Average interface radii vs. time (*left*) and percent symmetry errors vs. time (*right*) for the 3D spherical shell collapse problem using a Q_2 - Q_1 method on a sequence of refined meshes.

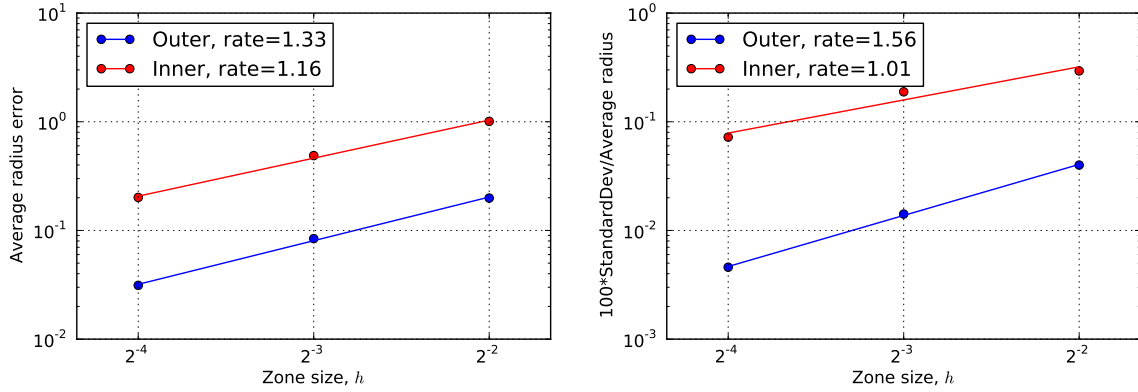


Figure 16: Convergence rates for the average radii (*left*) and percent symmetry errors (*right*) at the final time for the 3D spherical shell collapse using a Q_2 - Q_1 method with h -refinement.

- [23] D. J. Steinberg. Equation of state and strength properties of selected materials. Technical Report UCRL-MA-106439, Lawrence Livermore National Laboratory, 1996.
- [24] BLAST: High-order finite element shock hydrocode. <http://www.llnl.gov/CASC/blast>.
- [25] MFEM: Modular parallel finite element methods library. <http://mfem.googlecode.com>.
- [26] M. Kennamond and T. McAbee. Personal communication, 2011. LLNL.
- [27] G. Bazan. Personal communication, 2010. LLNL.
- [28] D. Verney. Evaluation de la limite elastique du cuivre et de l'uranium par des experiences d'implosion 'lente'. In *Behavior of Dense Media Under High Dynamic Pressures, Symposium, H.D.P., IUTAM*, pages 293–303, Paris, 1968. Gordon and Breach, New York.

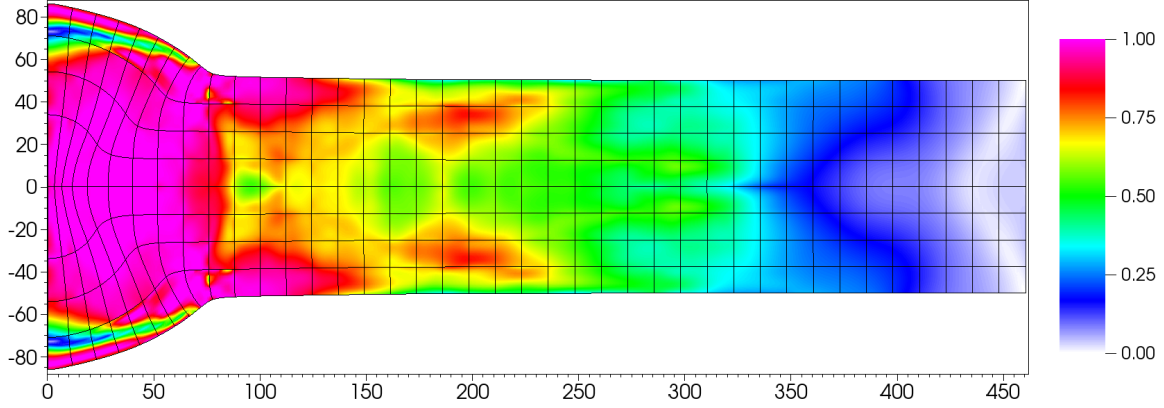


Figure 17: Pseudocolor plot of plasticity threshold and curvilinear mesh for the 2D impact problem on a 40 by 8 2D mesh using a Q_4 - Q_3 method.

- [29] J. R. Kamm, J. S. Brock, S. T. Brandon, D. L. Cotrell, B. M. Johnson, P. Knupp, T. G. Trucano, W. J. Rider, and V. G. Weirs. Enhanced verification test suite for physics simulations codes. Technical Report SAND2008-7813, Sandia National Laboratory, 2009.
- [30] D.E. Burton, T.C. Carney, N.R. Morgan, S.K. Sambasivan, and M.J. Shashkov. A cell-centered lagrangian godunov-like method for solid dynamics. *Computers and Fluids*, 2012. in press, doi:10.1016/j.compfluid.2012.09.008.

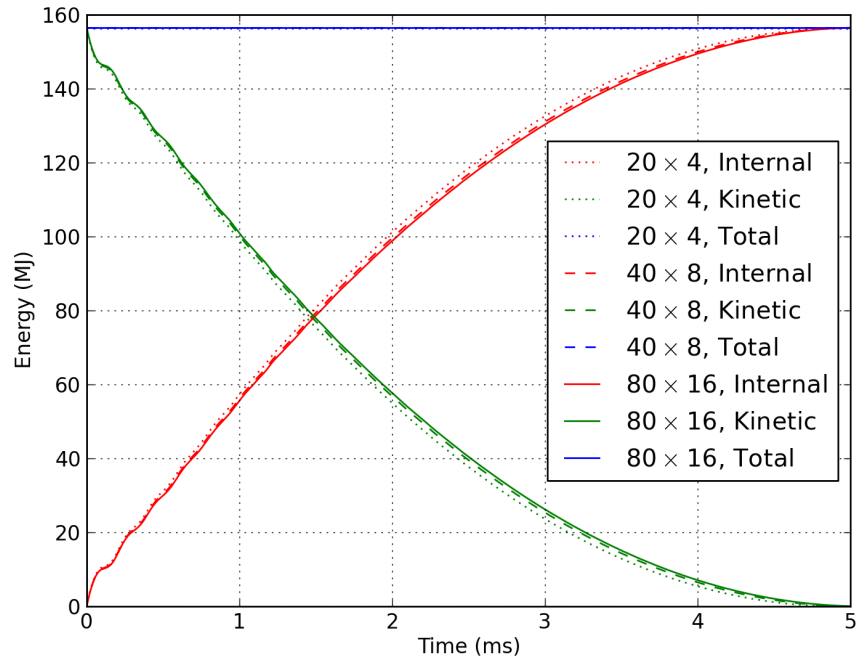


Figure 18: Total, kinetic and internal energies vs. time for the 2D impact problem using a Q_4 - Q_3 method on a sequence of refined meshes.

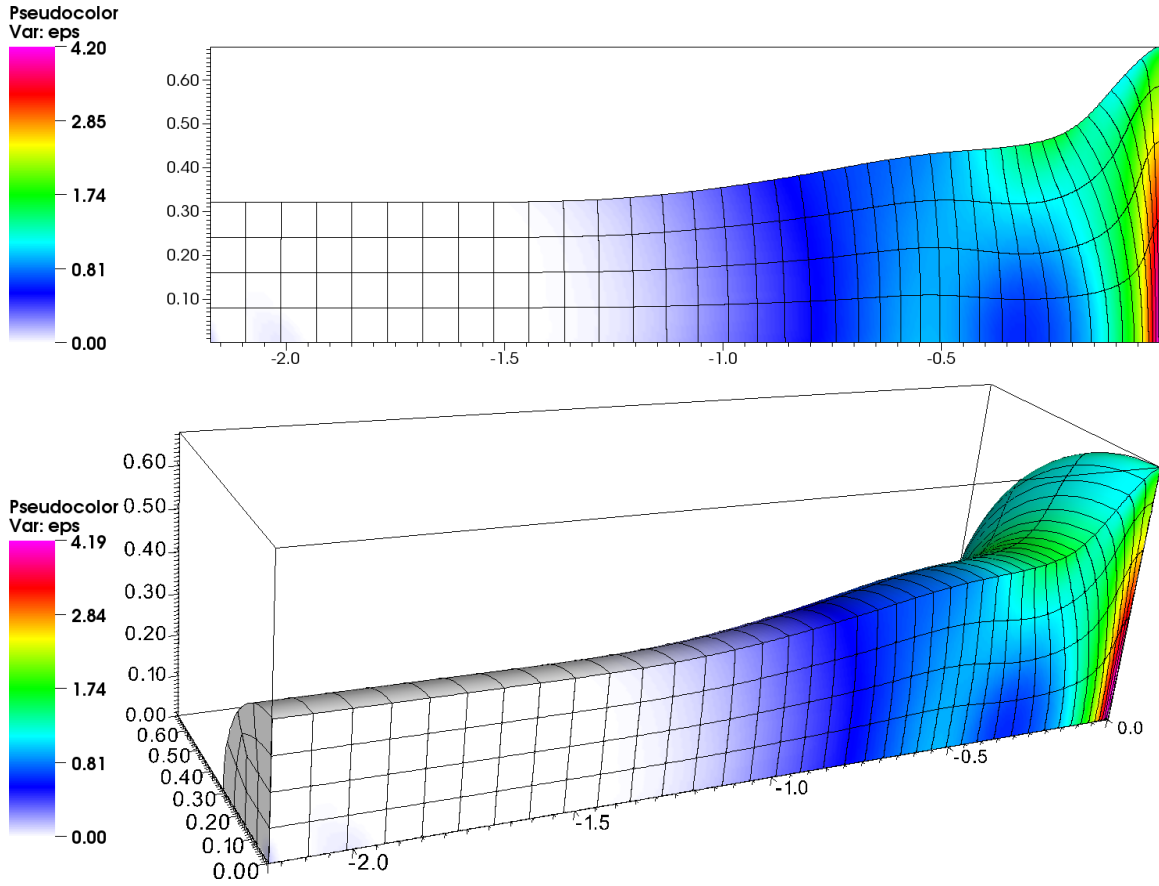


Figure 19: Pseudocolor plot of equivalent plastic strain and curvilinear mesh for the Taylor impact problem using a 2D (r, z) Q_4 - Q_3 method (*top*) and a 3D Q_4 - Q_3 method (*bottom*) at time $t = 80$.

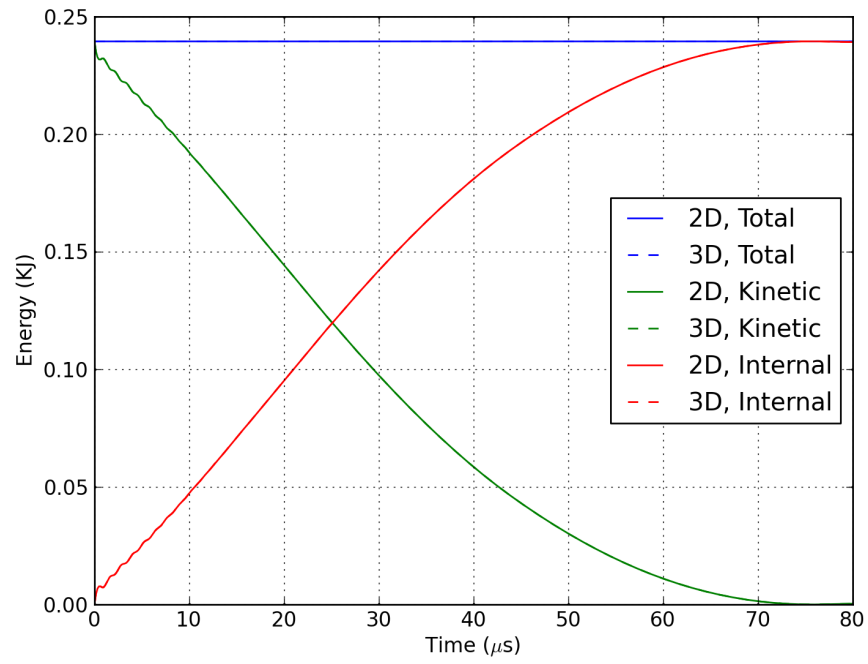


Figure 20: Total, kinetic and internal energies vs. time for the Taylor impact problem using a 2D (r, z) Q_4 - Q_3 method and a 3D Q_4 - Q_3 method.